The Astrophysical Journal, 852:100 (13pp), 2018 January 10 https://doi.org/10.3847/1538-4357/aaa01f

Early Observations of the Type Ia Supernova iPTF 16abc: A Case of Interaction with Nearby, Unbound Material and/or Strong Ejecta Mixing

A. A. Miller[1,2], Y. Cao[3], A. L. Piro[4], N. Blagorodnova[5], B. D. Bue[6], S. B. Cenko[7,8], S. Dhawan[9], R. Ferretti[9], O. D. Fox[10], C. Fremling[11], A. Goobar[9], D. A. Howell[12,13], G. Hosseinzadeh[12,13], M. M. Kasliwal[5], R. R. Laher[14], R. Lunnan[5], F. J. Masci[14], C. McCully[12,13], P. E. Nugent[15,16], J. Sollerman[11], F. Taddia[11], and S. R. Kulkarni[5]

[1] Center for Interdisciplinary Exploration and Research in Astrophysics (CIERA) and Department of Physics and Astronomy, Northwestern University, 2145 Sheridan Road, Evanston, IL 60208, USA; amiller@northestern.edu
[2] The Adler Planetarium, Chicago, IL 60605, USA
[3] eScience Institute and Astronomy Department, University of Washington, Seattle, WA 98195, USA
[4] The Observatories of the Carnegie Institution for Science, 813 Santa Barbara Street, Pasadena, CA 91101, USA
[5] Division of Physics, Mathematics, and Astronomy, California Institute of Technology, Pasadena, CA 91125, USA
[6] Jet Propulsion Laboratory, California Institute of Technology, Pasadena, CA 91109, USA
[7] NASA Goddard Space Flight Center, Mail Code 661, Greenbelt, MD 20771, USA
[8] Joint Space-Science Institute, University of Maryland, College Park, MD 20742, USA
[9] The Oskar Klein Centre, Department of Physics, Stockholm University, AlbaNova, SE-106 91 Stockholm, Sweden
[10] Space Telescope Science Institute, 3700 San Martin Drive, Baltimore, MD 21218, USA
[11] The Oskar Klein Centre, Department of Astronomy, Stockholm University, AlbaNova, SE-106 91 Stockholm, Sweden
[12] Las Cumbres Observatory, Goleta, CA 93117, USA
[13] Physics Department, University of California, Santa Barbara, CA 93106, USA
[14] Infrared Processing and Analysis Center, California Institute of Technology, Pasadena, CA 91125, USA
[15] Lawrence Berkeley National Laboratory, Berkeley, CA 94720, USA
[16] University of California—Berkeley, Berkeley, CA 94720, USA
Received 2017 August 23; revised 2017 November 23; accepted 2017 December 5; published 2018 January 11

Abstract

Early observations of Type Ia supernovae (SNe Ia) provide a unique probe of their progenitor systems and explosion physics. Here we report the intermediate Palomar Transient Factory (iPTF) discovery of an extraordinarily young SN Ia, iPTF 16abc. By fitting a power law to our early light curve, we infer that first light for the SN, that is, when the SN could have first been detected by our survey, occurred only $0.15\pm^{0.15}_{0.07}$ days before our first detection. In the ∼24 hr after discovery, iPTF 16abc rose by ∼2 mag, featuring a near-linear rise in flux for $\gtrsim$3 days. Early spectra show strong C II absorption, which disappears after ∼7 days. Unlike the extensively observed Type Ia SN 2011fe, the $(B-V)_0$ colors of iPTF 16abc are blue and nearly constant in the days after explosion. We show that our early observations of iPTF 16abc cannot be explained by either SN shock breakout and the associated, subsequent cooling or the SN ejecta colliding with a stellar companion. Instead, we argue that the early characteristics of iPTF 16abc, including (i) the rapid, near-linear rise, (ii) the nonevolving blue colors, and (iii) the strong C II absorption, are the result of either ejecta interaction with nearby, unbound material or vigorous mixing of radioactive ^{56}Ni in the SN ejecta, or a combination of the two. In the next few years, dozens of very young *normal* SNe Ia will be discovered, and observations similar to those presented here will constrain the white dwarf explosion mechanism.

Key words: methods: observational – supernovae: general – supernovae: individual (iPTF 16abc; SN 2011fe) – surveys

1. Introduction

Although Type Ia supernovae (SNe Ia) have been extensively used as standardizable candles, their progenitor systems and explosion physics are still debated (see a recent review by Maoz et al. 2014). Extremely detailed observations in the hours to days after explosion provide a promising avenue to further constrain this problem.

While the shock breakout of an SN Ia occurs on a subsecond timescale, the subsequent quasi-adiabatic expansion and cooling of the unbound ejecta produces thermal emission that can be used to infer the radius of the exploding star (Piro et al. 2010; Rabinak & Waxman 2011). Comparing models of this cooling emission to the earliest-phase data of SN 2011fe, Bloom et al. (2012) concluded that the explosion came from a star with $R_* \lesssim 0.02\ R_\odot$, where $R_\odot$ is the solar radius. Combining the radius constraint with the measured ejecta mass, Bloom et al. derive the mean density of the progenitor star, confirming that at least some Type Ia SNe come from compact and degenerate stars.

Early-phase observations of SNe Ia from a white dwarf (WD)+nondegenerate binary may detect excess emission, relative to most SNe Ia, due to the collision of the SN ejecta with the nondegenerate companion (Whelan & Iben 1973; Kasen 2010). This excess emission was first detected in iPTF 14atg (Cao et al. 2015), a low-velocity SN Ia with a significant and declining ultraviolet (UV) pulse detected within a few days of the SN explosion. This UV pulse is best interpreted as an SN ejecta–companion collision (but see also Kromer et al. 2016; Noebauer et al. 2017). While such emission requires a favorable geometric alignment and is only expected in $\lesssim$10% of SNe Ia (Kasen 2010), many studies have searched for signatures of an ejecta–companion interaction, typically resulting in nondetections (e.g., Hayden et al. 2010a; Bianco et al. 2011; Bloom et al. 2012; Foley et al. 2012; Zheng et al. 2013; Goobar et al. 2015; Im et al. 2015; Olling et al. 2015; Shappee et al. 2016a). Possible exceptions include SN 2012cg, which exhibited excess blue emission in its early-phase light curve (Marion et al. 2016; though for an interpretation that does

not invoke ejecta–companion interaction, see Shappee et al. 2016b), and SN 2017cbv, which shows a clearly resolved "bump" in the early *UBg* light curves (Hosseinzadeh et al. 2017).

Interaction is not limited to systems with a nondegenerate companion, however, as WDs enshrouded in diffuse material following a binary merger (e.g., Levanon et al. 2015) or expanded owing to a pre-explosion pulsation can give rise to ejecta-interaction signatures (e.g., Dessart et al. 2014). Models of this scenario naturally produce C II absorption that is comparable in strength to Si II in the days after explosion (Dessart et al. 2014), as was observed in SN 2013dy (Zheng et al. 2013) and SN 2017cbv (Hosseinzadeh et al. 2017).

The vast majority of SNe Ia are observed to be powered purely by the radioactive decay of ^{56}Ni. While the detection of SN shock cooling or ejecta interaction is rare, the level of ^{56}Ni mixing in the SN ejecta can fundamentally alter the appearance of the SN shortly after explosion (e.g., Dessart et al. 2014; Piro & Morozova 2016; Noebauer et al. 2017).

SNe Ia experience a dark phase after the SN shock breakout but before radioactive energy diffuses into the photosphere (Piro & Nakar 2014). The duration of this dark phase is set by how the newly synthesized ^{56}Ni is mixed and deposited into different layers of the ejecta. Strong mixing leads to a short, or nonexistent, dark phase, because the radioactive γ-rays rapidly diffuse to the photosphere. This also leads to larger luminosities and bluer optical colors at early times. Even with vigorous mixing it is difficult at very early times, $\ll$1 day after explosion, to explain very large luminosities or blue colors, because the ^{56}Ni has not had sufficient time to radioactively decay to ^{56}Co. If the mixing is weak and the ^{56}Ni is confined to the innermost layers of the ejecta, the dark phase can last several days. Weak mixing results in redder colors and a more moderate rise in luminosity (Dessart et al. 2014; Piro & Morozova 2016). Thus, the early light curves of even nonexotic SNe Ia convey information about their progenitor systems and explosion mechanisms by constraining the distribution of ^{56}Ni.

Noebauer et al. (2017) demonstrate that disambiguating between these different scenarios via optical photometry alone is challenging. Noebauer et al. further show that estimates of the time of explosion, which are critical for comparing models with observations, are often incorrect by as much as $\sim$2 days using common methods in the literature. While analytical models suggest that early spectra can be used to infer the time of explosion (e.g., Piro & Nakar 2014), more detailed simulations show that the photospheric evolution is not so simple (Piro & Morozova 2016). Reconciling these issues requires both a larger sample of early SN Ia observations and more detailed models that produce synthetic light curves and spectra.

In this paper, we report observations of an extraordinarily young SN Ia, iPTF 16abc, which was discovered by the intermediate Palomar Transient Factory (iPTF) on 2016 April 3.36 UTC at R.A. $= 13^{\rm h}34^{\rm m}45\overset{\rm s}{.}49$, decl. $= +13°51'14\overset{''}{.}3$ (J2000) with a $g_{\rm PTF}$-band magnitude of 21.44 $\pm$ 0.25 (Miller et al. 2016). The transient is spatially coincident with a tidal tail of the galaxy NGC 5221, which lies at a distance of $\sim$100 Mpc. iPTF 16abc is not detected to a 5σ limit of $g_{\rm PTF} = 21.9$ mag on April 2.42, less than 1 day prior to discovery, and rose by $\sim$2 mag in the 24 hr following its initial detection. Our spectroscopic follow-up campaign classified iPTF 16abc as a normal SN Ia (Cenko et al. 2016). Our observations and analysis show that the early evolution of iPTF 16abc exhibited several distinct properties relative to SN 2011fe. We interpret those differences as arising from either strong ^{56}Ni mixing or ejecta interaction with nearby, unbound material, or a combination of the two. Alongside this paper, we have released our open-source analysis and all of the data utilized in this study. These are available online at https://github.com/adamamiller/iPTF16abc.

2. Observations

During the spring of 2016, the iPTF survey observed the field of iPTF 16abc every night during dark time in either the $g_{\rm PTF}$ or $R_{\rm PTF}$ band.[17] Survey observations were conducted with the CFH12K camera (Rahmer et al. 2008) on the Palomar Observatory 48-inch telescope (P48; Law et al. 2009). Images were processed by the IPAC image-subtraction pipeline, which subtracts background galaxy light using deep pre-SN images and performs forced point-spread function (PSF) photometry at the location of the SN (Masci et al. 2017). The photometry is then calibrated to the PTF photometric catalog (Ofek et al. 2012).

After discovery, g'-, r'-, and i'-band photometry was obtained with the SED Machine (SEDm; Blagorodnova et al. 2017) mounted on the Palomar Observatory 60-inch telescope (P60). We utilized the Fremling Automated Pipeline (`FPipe`; Fremling et al. 2016) to subtract galaxy light from the SEDm images using archival Sloan Digital Sky Survey (SDSS) images as a reference. This pipeline then performed forced-PSF photometry at the location of iPTF 16abc, which is calibrated to the SDSS catalog (Ahn et al. 2014).

The Las Cumbres Observatory (LCO) 1 m telescope network obtained *BV g′ r′i ′* photometry. PSF photometry was measured on these images using the `lcogtsnpipe` pipeline (Valenti et al. 2016). The *BV* magnitudes are calibrated to the Fourth USNO CCD Astrograph Catalog (Zacharias et al. 2013), and the $g'r'i'$ magnitudes are calibrated to SDSS Data Release 6 (Adelman-McCarthy et al. 2008).

The Reionization and Transients InfraRed (RATIR) camera on the autonomous 1.5 m Harold L. Johnson Telescope (Butler et al. 2012; Watson et al. 2012) was used to observe iPTF 16abc in the *r′ i′ ZYJH* filters. By design, RATIR lacks a cold shutter, which means that IR dark frames are not available. Laboratory testing, however, confirms that the dark current is negligible in both IR detectors (Fox et al. 2012).

The RATIR data were reduced, co-added, and analyzed using standard CCD and IR processing techniques in `IDL`, `Python`, `SExtractor` (Bertin & Arnouts 1996), and `SWarp`. Aperture photometry is obtained following the methods described in Littlejohns et al. (2014). The *r′ i′ Z* filters are calibrated to SDSS (Ahn et al. 2014), while the *JH* filters are calibrated to the Two Micron All Sky Survey (Skrutskie et al. 2006). For the *Y*-band calibration, we used an empirical relation in terms of the *J* and *H* magnitudes derived from the United Kingdom Infrared Telescope (UKIRT; Casali

[17] P48 observations of iPTF 16abc are reported in the $g_{\rm PTF}$ and $R_{\rm PTF}$ filters throughout, which are similar to the SDSS g' and Mould-*R* filters, respectively (see Ofek et al. 2012, for details on PTF calibration). The correction from the $g_{\rm PTF}$ and $R_{\rm PTF}$ filters to SDSS g' and r' requires knowledge of the intrinsic source color (see Equations (1) and (2) in Ofek et al. 2012). The spectral diversity of SNe Ia in the days after explosion is poorly constrained, and as a result the color terms for iPTF 16abc at these epochs are unknown. We proceed by assuming that the $g_{\rm PTF}$ and $R_{\rm PTF}$ calibration is on the AB system, which strictly speaking is incorrect, but this does not fundamentally alter any of our conclusions.

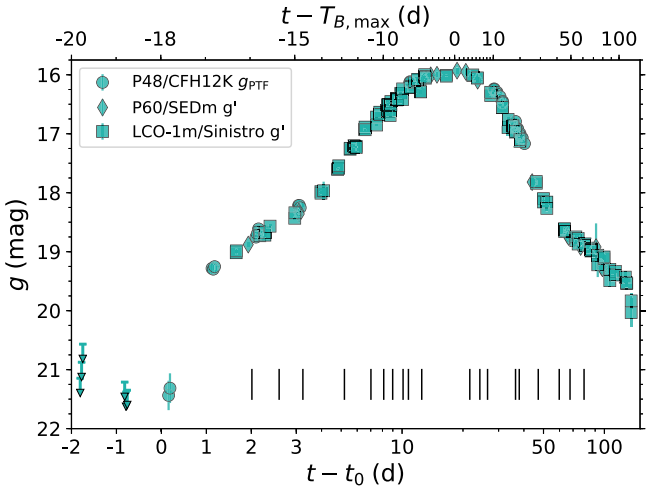

Figure 1. The g-band light curve of iPTF 16abc, with 5σ upper limits shown as downward-pointing arrows. Observations from different telescopes are shown with different symbols. The lower axis shows time measured in rest-frame days relative to t_0 (see Section 4.1), while the upper axis shows time relative to B-band maximum. Note that the horizontal axis is shown with a linear scale for -2 days $\leqslant t - t_0 \leqslant 3$ days and a log scale for $t - t_0 > 3$ days. Vertical black ticks show epochs of spectroscopic observations.

et al. 2007) Wide Field Camera observations (Hodgkin et al. 2009).

The *Swift* satellite observed iPTF 16abc on 14 epochs, beginning ∼15 days pre-maximum light through ∼22 days post-maximum. The SN flux is measured via aperture photometry on Ultraviolet-Optical Telescope (UVOT) images via the usual procedures in `HEASoft`, including corrections for coincidence loss and aperture loss. The image counts are converted to physical fluxes using the latest calibration (Breeveld et al. 2011). There are no pre-SN UVOT images at the SN location in the *Swift* archive. Visual inspection of the UVOT images suggests negligible host galaxy contamination in our UVOT flux measurements. No X-ray emission is detected from iPTF 16abc by the *Swift* X-ray Telescope (XRT).

The g-band discovery and follow-up data of iPTF 16abc are illustrated in Figure 1. The photometry is shown in the AB system. As previously noted, the color terms necessary to convert $g_{\rm PTF}$ to the AB system are unknown and assumed to be zero.

Spectroscopic observations of iPTF 16abc were taken with a variety of telescopes and instruments over multiple epochs beginning ∼2 days after discovery and ending ∼2 months after B-band maximum. An observing log is listed in Table 1. The spectra were reduced using standard procedures in `IDL/Python/Matlab`. The optical spectral evolution of iPTF 16abc is illustrated in Figure 2, which excludes high-resolution Very Large Telescope (VLT) spectra for clarity.

3. Host Galaxy, Reddening, and Classification

3.1. Host Galaxy

iPTF 16abc is spatially coincident with a tidal tail of galaxy NGC 5221. Theureau et al. (2007) derived a distance modulus of 35.0 ± 0.4 mag to NGC 5221 from the Tully–Fisher relation, consistent with our derivation from the SN light curve (see Section 3.3).

Table 1
Spectroscopic Observations of iPTF 16abc

Observation MJD	SN Phase	Telescope	Instrument	Range (Å)
57,483.26	−15.9	DCT	DeVeny[a]	3301–7499
57,483.88	−15.3	Gemini-north	GMOS[b]	3800–9200
57,484.51	−14.7	Keck-II	DEIMOS[c]	5500–8099
57,486.51	−12.7	Keck-II	DEIMOS[c]	5500–8099
57,488.38	−10.9	Keck-I	LRIS[d]	3055–10411
57,489.51	−9.8	LCO-2 m	FLOYDS[e]	3301–8999
57,490.40	−8.9	LCO-2 m	FLOYDS[e]	3301–9999
57,491.55	−7.8	LCO-2 m	FLOYDS[e]	3300–9998
57,492.20	−7.2	VLT	X-shooter[f]	3300–24550
57,494.00	−5.4	VLT	UVES[g]	
57,503.32	+3.7	LCO-2 m	FLOYDS[e]	3300–9999
57,506.00	+6.3	NOT	ALFOSC[h]	3602–8098
57,508.27	+8.5	LCO-2 m	FLOYDS[e]	3301–9999
57,518.42	+18.5	Keck-I	LRIS[d]	3071–10208
57,520.03	+20.0	VLT	X-shooter[f]	3300–24789
57,529.40	+29.2	LCO-2 m	FLOYDS[e]	4000–8998
57,542.41	+41.9	LCO-2 m	FLOYDS[e]	4000–8998
57,550.40	+49.7	LCO-2 m	FLOYDS[e]	4001–8999
57,562.38	+61.4	LCO-2 m	FLOYDS[e]	4800–9300

Notes.
[a] The Deveny Spectrograph (Bida et al. 2014).
[b] The Gemini Multi-Object Spectrograph (Hook et al. 2004).
[c] DEep Imaging Multi-Object Spectrograph (Faber et al. 2003).
[d] Low-Resolution Imaging Spectrometer (Oke et al. 1995).
[e] FLOYDS; https://lco.global/observatory/instruments/floyds.
[f] X-shooter (Vernet et al. 2011).
[g] Ultraviolet and Visual Echelle Spectrograph (Dekker et al. 2000).
[h] The Andalucia Faint Object Spectrograph and Camera; http://www.not.iac.es/instruments/alfosc.

Separately, Courtois & Tully (2015) observe the 21 cm line in NGC 5221 and measure a redshift of 0.0234, which we adopt for the remaining analysis in this paper.

3.2. Reddening

A detailed study of the reddening toward iPTF 16abc is presented in a companion paper (Ferretti et al. 2017). Briefly, the foreground Galactic extinction toward iPTF 16abc is $E(B-V) = 0.0279$ mag (Schlafly & Finkbeiner 2011). High-resolution spectra of iPTF 16abc show multiple absorption components for both the Ca II H+K and Na I D doublets. Despite large equivalent widths (EWs) for these lines, implying significant extinction (e.g., Poznanski et al. 2012), Ferretti et al. find evidence for only a small amount of extinction. The empirical relation between the EW of Na I D and extinction has a large scatter, and Phillips et al. (2013) have shown that Na I D absorption is a poor tracer of reddening in SNe Ia. Thus, we adopt $E(B-V) = 0.05$ mag as the local extinction for iPTF 16abc (Ferretti et al. 2017). For the remainder of our analysis we assume a total, Galactic+host galaxy, line-of-sight extinction of $E(B-V) = 0.08$ mag.

3.3. Classification

Using the SuperNova IDentification (`SNID`; Blondin & Tonry 2007) package, we find that the low-resolution spectrum of iPTF 16abc at +18.8 days is best matched by normal SNe Ia. Several characteristic features of an SN Ia, such as Si II and S II, can be easily identified in iPTF 16abc

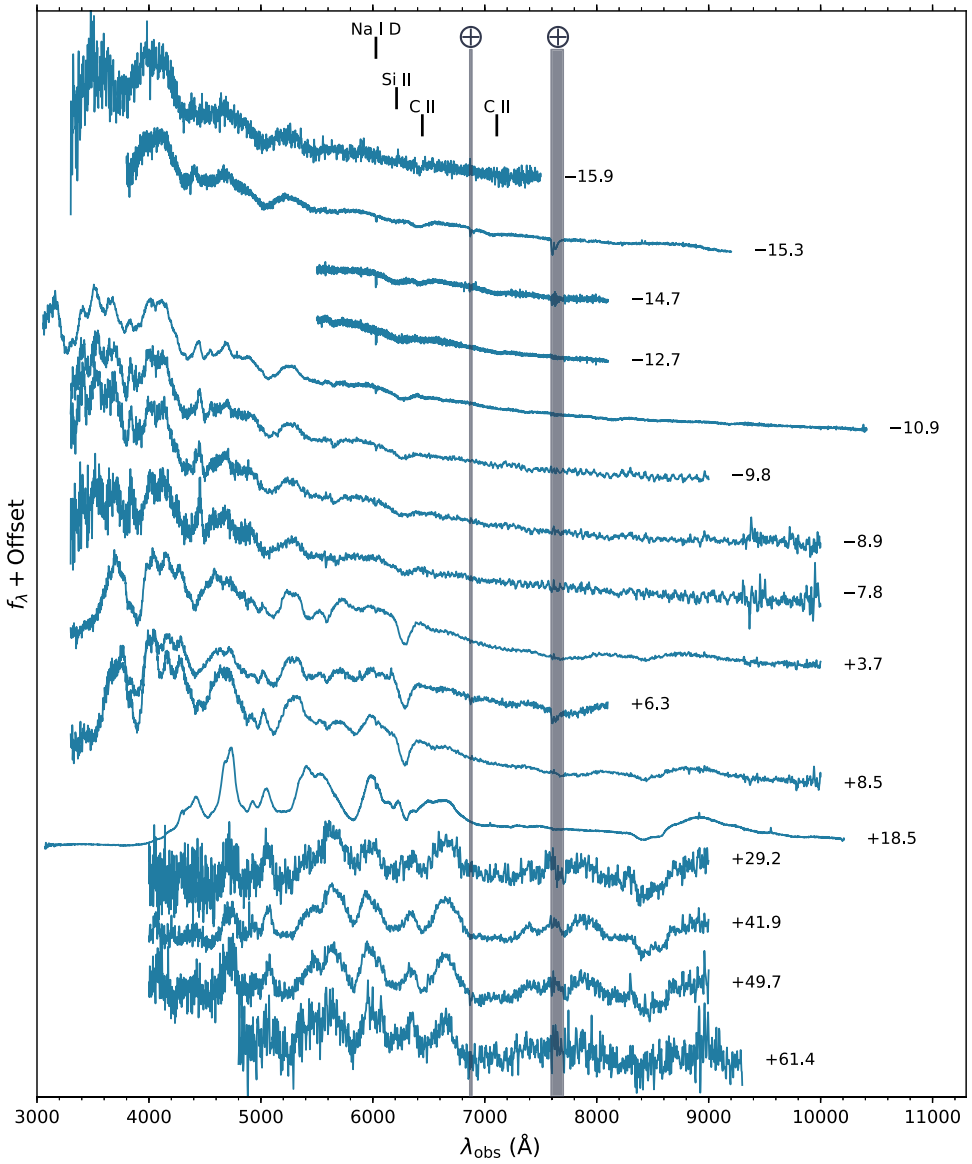

Figure 2. Observed spectral sequence of iPTF 16abc. The spectra are normalized by their median flux between 6000 and 7000 Å. The phase of each spectrum relative to the time of *B*-band maximum is shown. Telluric absorption bands are grayed out. Line identifications are provided for the spectral features discussed in the text. For clarity, high-resolution spectra obtained with the VLT have been omitted (see Ferretti et al. 2017, for a detailed discussion of these spectra).

(Figure 2). From the +3.7-day LCO spectrum, we measure pseudo-equivalent widths (pEWs) of -12 ± 2 Å and -55 ± 5 Å for the absorption features near 5750 and 6100 Å, attributed to Si II $\lambda\lambda$ 5972, 6355, respectively. According to the Branch et al. (2006) classification scheme, iPTF 16abc is a shallow-silicon SN, similar to 1999aa-like SNe (Branch et al. 2009). In Figure 3, the velocity evolution of the iPTF 16abc Si II λ6355 absorption minimum is compared to the median evolution of the four spectroscopic subclasses from Branch et al. (2006). The median evolution is defined using the sample of SNe Ia in Blondin et al. (2012). For each SN, we interpolate the Si II velocity, $v_{\mathrm{Si\ II}\ \lambda6355}$, to a fixed grid at 1-day intervals. The curves are defined by the median $v_{\mathrm{Si\ II}\ \lambda6355}$ at each point on the grid with at least three SNe (this prevents just one or two SNe from defining the evolution of an entire subclass). The velocity evolution of iPTF 16abc is most reminiscent of the shallow-silicon subclass.

To determine the brightness and time of *B*-band maximum for iPTF 16abc, we fit the P60 light curves with the `sncosmo` software package.[18] This fit includes a `SALT2` template (Guy et al. 2007) that has been corrected for extinction using the Fitzpatrick (1999) reddening law, $R_V = 3.1$, and $E(B-V) = 0.08$ mag.

We determine the time of rest-frame *B*-band maximum to be $\mathrm{MJD_{max}} = 57{,}499.54 \pm 0.23$, the coefficient of the zeroth principle component $x_0 = 0.0086 \pm 0.0003$, the coefficient of the first principle component $x_1 = 0.96 \pm 0.15$, and the color term $c = 0.033 \pm 0.029$. The best-fit model also gives an unreddened apparent peak magnitude of $m_B^* = 15.80 \pm 0.04$ mag in the SN rest frame. In the following sections, we adopt $\mathrm{MJD_{max}} = 57499.54$ as the time of *B*-band maximum, $T_{B,\mathrm{max}}$, and phase $t = 0$.

We measure the (pseudo-)bolometric luminosity, L_{UVOIR}, of iPTF 16abc at peak via trapezoidal integration of the reddening-corrected flux from the UV, optical, and near-IR

[18] `sncosmo` is available at https://sncosmo.readthedocs.io.

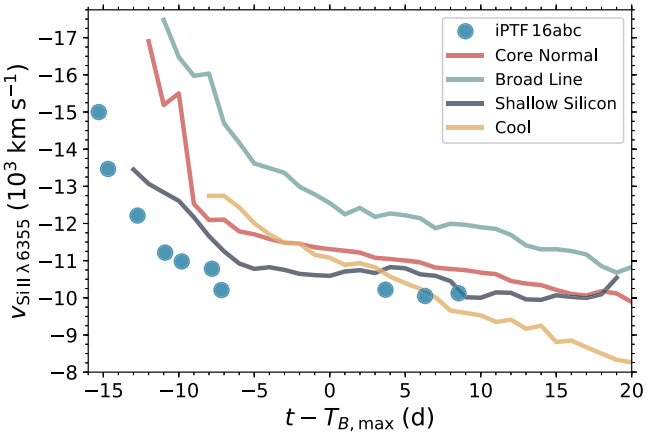

Figure 3. Velocity evolution of Si II, $v_{\rm Si\,II\,\lambda6355}$, for iPTF 16abc compared to the median evolution of the four spectroscopic subclasses defined in Branch et al. (2006), using data from Blondin et al. (2012). Typical uncertainties for iPTF 16abc are $\sim$1000 km s^{-1} before $T_{B,\rm max}$, when the Si II λ6355 profile is shallow and the minimum of absorption is difficult to determine, and $\sim$300 km s^{-1} after $T_{B,\rm max}$. For the median curves, the typical scatter, determined via the interquartile range of the sample, is $\sim$700 km s^{-1}, around $T_{B,\rm max}$. At early times, core-normal and broad-line SNe have significantly faster Si II than iPTF 16abc, while the declining trend of cool SNe does not match iPTF 16abc.

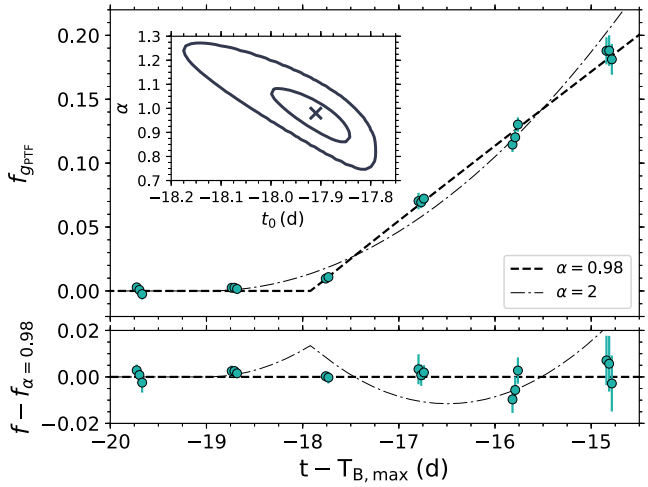

Figure 4. Best-fit $f \propto t^{\alpha}$ model to describe the early flux from iPTF 16abc in the $g_{\rm PTF}$ band. Top: the relative flux, $f_{g_{\rm PTF}}$ (shown as green circles), is measured via forced-PSF photometry. The model flux, adopting best-fit parameters $\alpha = 0.98$ and $t_0 = -17.91$ days, is shown as a thick dashed line. Also shown is the best-fit model after fixing $\alpha = 2$ (thin dot-dashed line). The inset shows the joint distribution of t_0 and α for the best-fit power-law model. The solid contours represent the 68% and 99.7% confidence levels. Bottom: observations and models following subtraction of the best-fit power-law model, $f_{\alpha=0.98}$. The $t^{0.98}$ model provides a much better fit to the observations than the t^2 model.

(UVOIR) filters. The light curves in the individual filters are interpolated so that $L_{\rm UVOIR}$ is evaluated at common epochs in each filter. From this integration, we measure a maximum luminosity $L_{\rm max} = 1.2 \pm 0.1 \times 10^{43}$ erg s^{-1} for iPTF 16abc. This value is consistent with the normal SNe Ia studied in Dhawan et al. (2016). Following Arnett's rule (Arnett 1982; Arnett et al. 1985), the mass of ^{56}Ni synthesized in the explosion can be derived from $L_{\rm max}$. Assuming a rise time of 19 ± 3 days (see Stritzinger et al. 2006), we find $M_{\rm Ni} = 0.6 \pm 0.1 M_{\odot}$.[19]

After establishing iPTF 16abc as a normal SN Ia, we use the latest calibration (Betoule et al. 2014) of the Phillips relation (Phillips 1993) using m_B^*, x_1, and c to derive a distance modulus $\mu = 34.89 \pm 0.10$ mag to the SN, provided that the host galaxy of iPTF 16abc has a stellar mass $<10^{10} M_{\odot}$. A more massive host galaxy would result in a larger inferred distance modulus that is nevertheless consistent within the uncertainties. For the following analysis we adopt a distance modulus $\mu = 34.89 \pm 0.10$ mag for iPTF 16abc.[20]

4. Early Observations

Here we consider our suite of early observations of iPTF 16abc and compare our findings with SN 2011fe, a well-studied, nearby SN that was discovered shortly after explosion (Nugent et al. 2011; Bloom et al. 2012; Piro & Nakar 2014).

4.1. Time of First Light from the Early Light Curve

The time of first light for SNe is usually estimated by extrapolating early-phase light curves to determine when the SN flux is equal to 0. Assuming an ideal, expanding fireball with constant temperature, Arnett (1982) derives that $f \propto t^2$, where f is the SN flux and t is the time since explosion. Despite these simplified assumptions, multiple studies have found that the early emission from SNe Ia can be described as a power law in time, with power-law index consistent with 2, i.e., $f \propto t^2$ (e.g., Conley et al. 2006; Hayden et al. 2010b; Ganeshalingam et al. 2011).[21]

We model the early flux from iPTF 16abc as a power law:

$$f(t) \begin{cases} =0, & \text{when } t \leqslant t_0 \\ \propto (t - t_0)^{\alpha}, & \text{when } t > t_0 \end{cases}, \quad (1)$$

where t_0 is the time of first light, α is the power-law index, and t is measured in the SN rest frame. We allow α to vary to find the best match to the data, and we later show that $\alpha = 2$ is not compatible with the observations. To determine t_0 and α, we fit the earliest observations of iPTF 16abc. Due to slight variations in the passbands, the model is fit only to the relative $g_{\rm PTF}$-band flux. $g_{\rm PTF}$ is the only filter with observations prior to first light, a necessity for constraining t_0.

To determine the best-fit parameters, we search a large grid over t_0, α, and the proportionality constant and minimize χ^2. The modeling results show that the SN flux rises approximately linearly between $t = -18$ days and $t = -15$ days. Figure 4 shows the best-fit result and the joint marginal distribution of t_0 and α. From the best-fit model we obtain $\alpha = 0.98^{+0.16}_{-0.14}$ and $t_0 = -17.91^{+0.07}_{-0.15}$ days, where the uncertainties represent the marginalized 95% confidence intervals. Our first detection of iPTF 16abc occurred $\sim$0.15 days after t_0. In the analysis that follows, the precise values of the best-fit parameters are not important. The critical finding here is that $\alpha \approx 1$ and $t_0 \approx -18$ days.

[19] A 17.9-day rise time (Section 4.1) yields a consistent estimate of $M_{\rm Ni}$.

[20] This μ is consistent with the $z_{\rm SN}$, $H_0 = 73$ km s^{-1} Mpc^{-1}, and Virgo-infall-corrected distance (Mould et al. 2000).

[21] Many of these studies sample SN Ia light curves at phases closer to $T_{B,\rm max}$ than our initial observations of iPTF 16abc.

Figure 4 also shows the best-fit model while fixing $\alpha = 2$. The $f \propto t^2$ model does not match the observations. Formally, for the $\alpha = 2$ model $\chi^2 = 63.7$ with $\nu = 15$ degrees of freedom (dof), while $\chi^2 = 10.2$ with $\nu = 14$ dof for the $\alpha = 0.98$ model.

As previously noted, a precise determination of the rise time, $t_{\rm rise}$, of SNe Ia is challenging, as there may be a dark phase following explosion (Piro & Nakar 2014). Nevertheless, to be consistent with previous studies (e.g., Ganeshalingam et al. 2011), here we find $t_{\rm rise} = 17.91 \pm^{0.15}_{0.07}$ days based on our fit for t_0. We caution, however, that t_0 corresponds to the time when iPTF 16abc was first detectable by P48 and not the time of explosion.

Unlike iPTF 16abc, the early emission from SN 2011fe is well fit by an $f \propto t^2$ model (Nugent et al. 2011). Thus, the near-linear flux evolution observed in iPTF 16abc is distinct compared to SN 2011fe. To our knowledge this behavior has only been observed in two other SNe (SN 2013dy and SN 2014J; Zheng et al. 2013, 2014; Goobar et al. 2015). Any model to explain the observations of iPTF 16abc must account for this near-linear rise in the days after first light.

As a brief aside, we note that simulations presented in Noebauer et al. (2017) show that SN Ia explosion models do not evolve as a power law in time. Noebauer et al. demonstrate that $f \propto t^{\alpha}$ fits to simulated light curves result in glaring errors to the estimated explosion times. While caution is advised in Noebauer et al. (2017), we note that our primary aim with the power-law fit is to characterize α for iPTF 16abc compared to SN 2011fe.

4.2. Time of Explosion from the Photospheric Velocity

The time of explosion $t_{\rm exp}$ is not equal to t_0 (see above); thus, Piro & Nakar (2014) suggest that measurements of the photospheric velocity can determine $t_{\rm exp}$ given that the ejecta begin expanding from the moment of explosion. Assuming a constant opacity in the ejecta, Piro & Nakar find that the photospheric velocity evolves as $v_{\rm ph} \propto (t - t_{\rm exp})^{-0.22}$. Numerical experiments by Piro & Morozova (2016) find that the constant-opacity assumption strongly depends on the amount of ^{56}Ni mixing in the SN ejecta. As a result, the adoption of a $t^{-0.22}$ power-law model may not be valid for all SNe Ia. Nevertheless, we proceed on the assumption that iPTF 16abc experienced strong ^{56}Ni mixing (see Section 5.5), corresponding to the models that are best approximated as a $t^{-0.22}$ power law. We do this in part to compare with previous studies, though we caution that the inferred value of $t_{\rm exp}$ is subject to uncertainties related to ejecta mixing.

While the photospheric velocity is not easy to measure, line velocities of Si II or Ca II can be used as a proxy (Piro & Nakar 2014; Shappee et al. 2016a). In the case of iPTF 16abc, the Ca II IR triplet is very weak, likely due to high temperatures in the ejecta. Thus, we determine the photospheric velocity from the Si II λ6355 line. Visual inspection shows no sign of multiple-velocity components of Si II and that the C II λ6580 line overlaps the red wing of the Si II line (see Figures 2 and 6). Consequently, we model the observed spectra between 5900 and 6500 Å (rest frame) as the combination of two Gaussian kernels plus a linear baseline, which accounts for Si II, C II, and the continuum, respectively. The expansion velocity of Si II is measured by the central wavelength of the Si II Gaussian kernel.

We fit the measured velocities of Si II λ6355 to the $v_{\rm ph} \propto (t - t_{\rm exp})^{-0.22}$ model by minimizing the χ^2 value and find the best-fit explosion time relative to $T_{B,\rm max}$ in the SN rest frame to be $t_{\rm exp} = -17.45 \pm^{0.14}_{0.16}$ days, where the uncertainties represent the 95% confidence interval (Figure 5). Following the analysis in Piro & Nakar (2014), we additionally alter the power-law index to -0.20 and -0.24 to examine the sensitivity of the result on the assumed value of -0.22. We find that this variation in the power-law index results in a change of $t_{\rm exp}$ of $\approx \pm$ 0.5 days (Figure 5). Given the analytical approximation that $v_{\rm ph} \propto t^{-0.22}$, we adopt $t_{\rm exp} = -17.5 \pm 0.5$ days, where the uncertainty reflects possible variations in the power-lax index (see Piro & Nakar 2014).

Comparing our estimates for $t_{\rm exp}$ and t_0 (Figure 5), we find that $t_0 \lesssim t_{\rm exp}$. Since physical causality requires $t_{\rm exp} \leqslant t_0$, we draw the qualitative conclusion that $t_0 \simeq t_{\rm exp}$, which is consistent to within the uncertainties. This derivation of $t_{\rm exp}$ relies on the assumption $v_{\rm ph} \propto t^{-0.22}$, which may not be valid for all SNe Ia.

4.3. Strong and Short-lived Carbon Features

The early spectra of iPTF 16abc exhibit unusually strong C II $\lambda\lambda$6580, 7234 absorption. The evolution of these spectral features is highlighted in Figure 6, which shows that C II λ6580 is as strong as Si II λ6355 at $t \approx -15$ days. The strength of the C II lines declines with time, and by $t \approx -10$ days C II is no longer detectable.

Similar to our analysis of the Si II λ6355 line, we can measure velocities and pEWs of C II $\lambda\lambda$6580, 7234. We compare the velocity evolution of C II with that of Si II in the right panel of Figure 5, which also shows the pEWs of these lines. These measurements confirm the qualitative analysis from Figure 6, namely, the strength of C II λ6580 is similar to Si II λ6355 at $t \approx -16$ days before decreasing and eventually disappearing around $t = -10$ days.

The detection of C II in SN Ia spectra is relatively rare, as it requires both unburned carbon, which is likely only present in the outermost layers of the ejecta, and nonlocal thermal equilibrium effects in order to excite the ionized carbon (e.g., Thomas et al. 2007). Spectra obtained around or after $T_{B,\rm max}$ rarely show C II, as the photosphere has receded from the outermost ejecta, while pre-maximum spectra show evidence for weak C II absorption in $\sim 1/4$ of all normal SNe Ia (e.g., Parrent et al. 2011; Thomas et al. 2011; Silverman & Filippenko 2012). While the sample of SNe Ia with spectra taken within a few days of explosion is small, SN 2013dy and SN 2017cbv are the only other objects known to have strong C II features like iPTF 16abc (Zheng et al. 2013; Hosseinzadeh et al. 2017). As a counterexample, SN 2011fe only exhibited weak C II features in its first spectra (Parrent et al. 2012). Thus, models of iPTF 16abc must explain the strong C II absorption observed shortly after explosion.

4.4. Blue Optical Colors Shortly after Explosion

Multiband observations of iPTF 16abc began $\sim$1.5 days after discovery, which allows us to trace its color evolution starting $\sim$1.7 days after t_0. In Figure 7 we compare the $(B - V)_0$ color evolution of iPTF 16abc to observations of SN 2011fe

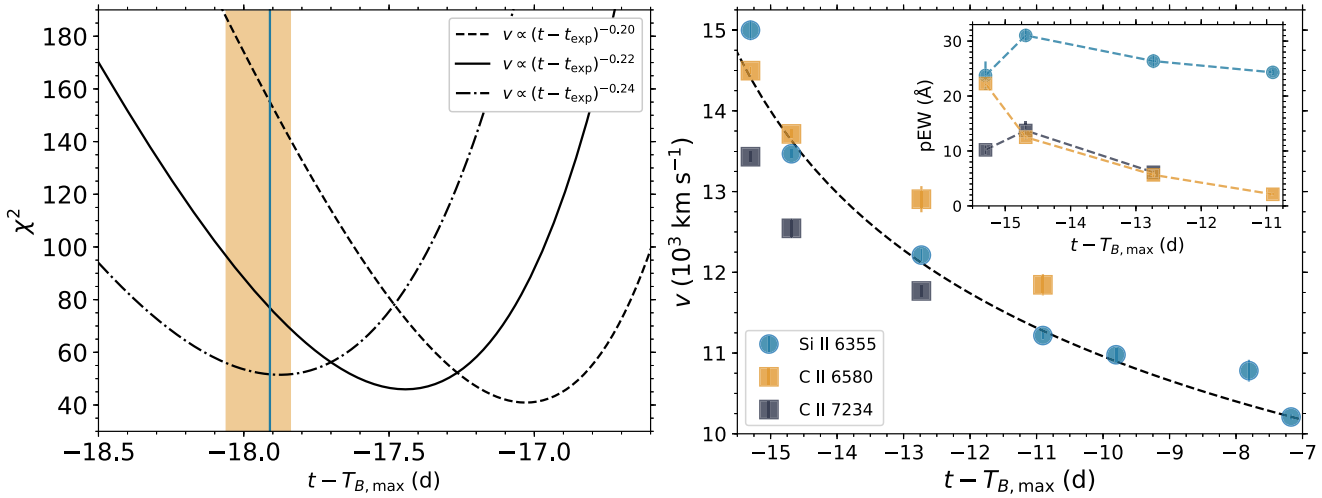

Figure 5. Constraints on $t_{\rm exp}$ from the velocity evolution of Si II. Left panel: the dashed, solid, and dot-dashed curves show χ^2 for fitting power laws with indices -0.20, -0.22, and -0.24, respectively. The blue vertical line and the orange shaded region indicate t_0 and its 95% confidence interval from Section 4.1, respectively. Right panel: observed Si II λ6355 velocities (blue circles) and the best-fit power-law model with an index of -0.22 (dashed line). For comparison, the measured velocities of C II $\lambda\lambda$ 6580, 7234 are also shown. Typical uncertainties are smaller than the size of the points. Right inset: evolution of the pseudo-equivalent width of Si II λ6355 and C II $\lambda\lambda$ 6580, 7234 in the $\sim$7 days following explosion.

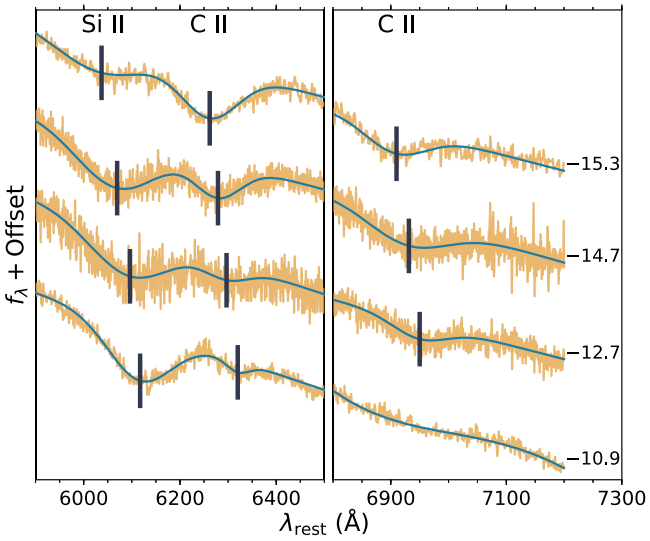

Figure 6. Evolution of the C II features observed in the early spectra of iPTF 16abc. The raw spectra are shown in orange, while the solid blue lines show the best-fit models (see text for further details). The dark gray vertical lines show the measured line centers and clearly show the decline in the photosphere velocity in the $\sim$7 days after explosion (C II λ7234 is not detected in the -10.9-day spectrum). The phase of each spectrum relative to $T_{B,\rm max}$ is labeled.

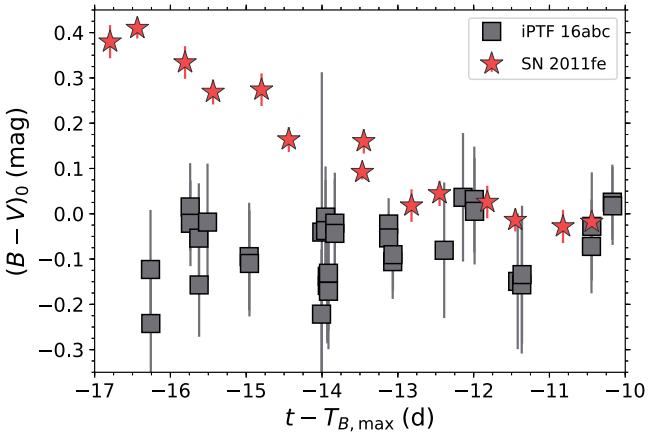

Figure 7. $(B - V)_0$ color evolution of iPTF 16abc (squares) compared to SN 2011fe (stars). The B and V photometry are calibrated on the Vega system, and have been corrected for extinction. The data for SN 2011fe are from Zhang et al. (2016).

(Zhang et al. 2016). For both SNe the colors have been corrected for the total inferred reddening along the line of sight. Interestingly, iPTF 16abc has a nearly flat color evolution up to $t \approx -10$ days, while SN 2011fe initially exhibits red colors before evolving to the blue.

Roughly 16 days prior to $T_{B,\rm max}$, the $(B - V)_0$ color of iPTF 16abc is $\sim$0.5 mag bluer than SN 2011fe. Like iPTF 16abc, SN 2012cg (Marion et al. 2016) and SN 2017cbv (Hosseinzadeh et al. 2017) exhibit $(B - V)_0$ colors that are significantly bluer than SN 2011fe at very early epochs. While there are many factors that contribute to the early optical colors of SNe Ia (see Section 5 below), early blue colors are often interpreted as a hallmark of interaction between the SN ejecta and a binary companion. Nevertheless, it is interesting to note that despite the blue optical colors, the UV–optical colors of iPTF 16abc, SN 2012cg, and SN 2017cbv are significantly redder at these early epochs than the UV–optical colors of iPTF 14atg (Cao et al. 2015), the most likely candidate for SN ejecta–companion interaction.

5. Modeling the Early Evolution of iPTF 16abc

Relative to the nearby, normal SN 2011fe, we have identified several distinct characteristics of the early evolution of iPTF 16abc, including (i) a near-linear photometric rise; (ii) a qualitatively short, or possibly absent, dark phase, assuming $v_{\rm ph} \propto t^{-0.22}$; (iii) the presence of strong C II absorption; and (iv) blue and nearly constant $(B - V)_0$ color in the week after explosion. While most SNe Ia are powered purely by radioactive decay, the observed radiation shortly after explosion can also include contributions from SN shock cooling or the collision of the SN ejecta with a nondegenerate companion or nearby, unbound material. Here we consider these scenarios as possible explanations for the early behavior of iPTF 16abc.

5.1. SN Shock Cooling

The shock breakout of an SN Ia lasts for a fraction of a second owing to the compact size of the exploding star. Emission from the subsequent cooling phase may last for several days, however (e.g., Piro et al. 2010). Following the analysis of Bloom et al. (2012) for SN 2011fe, we compare the early-phase $g_{\rm PTF}$ light curve of iPTF 16abc with two shock cooling models (Piro et al. 2010; Rabinak & Waxman 2011). From this analysis, we constrain the iPTF 16abc progenitor radius to be $<1\,R_{\odot}$. Our observations of iPTF 16abc cannot place tight constraints on the size of its progenitor. Indeed, for a typical WD radius, such as that inferred for SN 2011fe ($\lesssim$0.02–0.04 $R_{\odot}$; Bloom et al. 2012; Piro & Nakar 2014), the expected emission from shock cooling is $\sim$2 mag fainter than the P48 $g_{\rm PTF}$ detection limit at this distance. Thus, we conclude that shock cooling does not contribute to the early emission detected from iPTF 16abc.

5.2. SN–Companion Collision

The detection of emission from the collision of the SN ejecta with a nondegenerate companion requires a favorable orbital alignment relative to the line of sight. Thus, from geometric considerations alone the probability of detecting ejecta–companion interaction is low, $\sim$10%. Kasen (2010) calculates that the collision of SN ejecta with a companion generates thermal emission with a spectrum that peaks in the UV. The resulting g-band emission is expected to be weak.

To examine the possibility of an SN–companion signature in the early light curve of iPTF 16abc, we employ the Kasen (2010) model and assume canonical values for the ejecta mass, 1.4 $M_{\odot}$, expansion velocity, 10^4 km s^{-1}, and a constant opacity, 0.2 cm^2 g^{-1}. We calculate the expected $g_{\rm PTF}$ brightness of an ejecta–companion collision at the distance of iPTF 16abc behind a total reddening of $E(B-V)=0.08$ mag using the parameterized equations in Brown et al. (2012). If we assume that the binary is aligned with the optimal orientation relative to the line of sight, a binary separation of $a\approx 3\times10^{11}$ cm is needed to explain the initial detection of iPTF 16abc, as shown in Figure 8. The minimum binary separation capable of explaining the observed brightness at the epoch of discovery is $a\approx10^{11}$ cm. Figure 8 shows that such models peak at $g_{\rm PTF}\approx21.5$ mag, provided that $t_{\rm exp}\approx t_0-0.3$ days. These models do not, however, match the $g_{\rm PTF}$ evolution for $t>t_0+0.5$ days (though it is possible that the SN photosphere dominates the companion-interaction signature at this phase). While they are otherwise compatible with the observations, we do not favor the above models as the explanation for the early flux from iPTF 16abc because they do not explain the 2 mag rise in the $\sim$24 hr after discovery.

Figure 8 additionally shows that a companion at $a\approx18\times10^{11}$ cm provides a good match to the initial optical rise, if $t_{\rm exp}\approx t_0+0.1$ days. Models with $a\gtrsim10^{12}$ cm, which can explain the initial $g_{\rm PTF}$ rise, significantly overpredict the observed UV flux, however. There is no choice of a capable of replicating the early rise of iPTF 16abc without also overpredicting the observed UV flux.

The challenges associated with each of the previously considered models lead us to conclude that the early evolution of iPTF 16abc cannot be explained via ejecta–companion interaction. We cannot, however, exclude the presence of a red giant or other nondegenerate companion, as our calculations have assumed that the binary is aligned with the optimal geometry relative to the line of sight. If the geometry is not favorable, then it is possible that signatures from interaction with a companion are not visible.

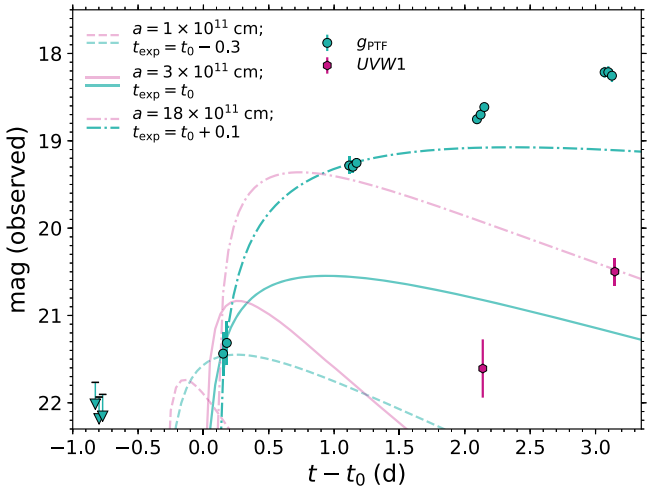

Figure 8. Comparison of SN ejecta–companion interaction models with early observations of iPTF 16abc. $g_{\rm PTF}$ detections and 3σ upper limits are shown as green circles and downward-pointing arrows, respectively. *Swift*/*UVW*1 observations are shown as magenta hexagons. The dashed, solid, and dot-dashed lines show the expected flux for companion-interaction models in the $g_{\rm PTF}$ (green) and *UVW*1 (magenta) filters. The models have been adjusted to account for the distance and reddening toward iPTF 16abc. Each model features a different companion semimajor axis, a, and time of explosion, $t_{\rm exp}$, as labeled in the legend. While models with $a\gtrsim10^{12}$ cm can explain the early optical rise, they greatly overpredict the UV flux. Models with $a\approx10^{11}$ cm can explain the initial detection of iPTF 16abc, but they fail to replicate the $\sim$2 mag rise in the $\sim$24 hr after explosion.

5.3. Sub-Chandrasekhar Detonations and Pure Deflagrations

In Noebauer et al. (2017) the early photometric evolution of SNe Ia is explored via a variety of explosion models and detailed radiative transfer calculations. Specifically, Noebauer et al. (2017) examine two Chandrasekhar-mass ($M_{\rm Ch}$) explosions and compare their evolution to sub-Chandrasekhar detonations and pure deflagrations. The $M_{\rm Ch}$ explosions include the "W7" carbon-deflagration model of Nomoto et al. (1984) and the "N100" delayed-detonation model from Seitenzahl et al. (2013). The sub-Chandrasekhar models include a violent WD–WD merger, which triggers a carbon detonation in the more massive WD, a centrally ignited sub-Chandrasehkar detonation, and a sub-Chandrasehkar double-detonation explosion, in which an He-surface-layer detonation triggers a carbon detonation in the core. Noebauer et al. (2017) note that, of these last two sub-Chandrasehkar models, the latter provides the more realistic scenario. Finally, Noebauer et al. also examine the "N5def" and "N1600Cdef" pure deflagration explosions from Fink et al. (2014). The "N5def" model is particularly unique in that the explosion does not fully unbind the WD, meaning that, unlike with typical SNe Ia, a remnant remains.

In Figure 9 we compare photometric observations of iPTF 16abc to the models presented in Noebauer et al. (2017).[22] Interestingly, the sub-Chandrasekhar double-detonation model (subChDoubleDet) replicates the early wiggle in the V-band light curve. However, this match requires an explosion *after* our initial detection of iPTF 16abc and predicts extreme color evolution that

[22] Available at https://hesma.h-its.org/.

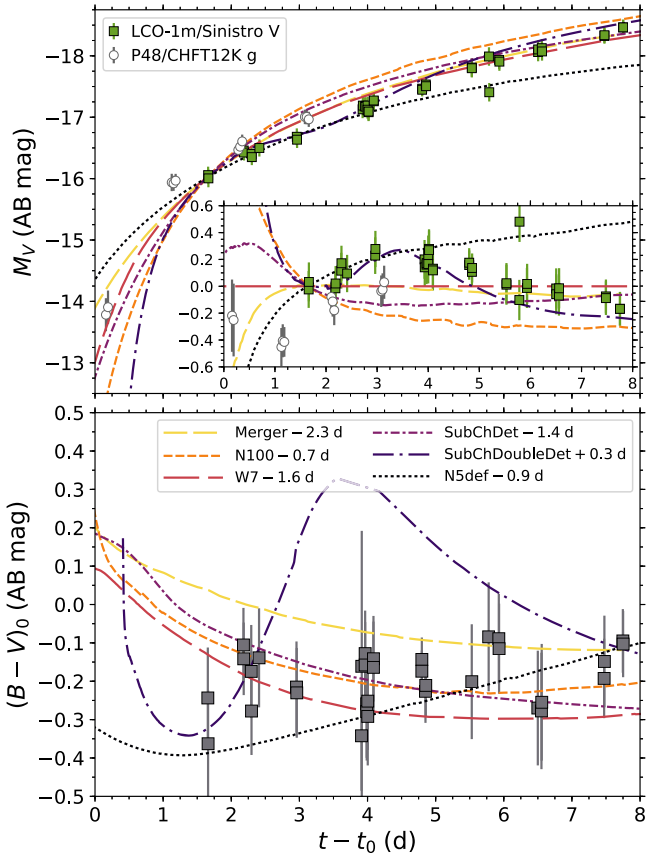

Figure 9. Comparison of the models from Noebauer et al. (2017) to the iPTF 16abc V-band light curve (top) and the $(B-V)_0$ color curve (bottom). The light curve has been corrected for the distance modulus to iPTF 16abc (Section 3.1), while both the light curve and color curve have been corrected for reddening. To guide the eye, $g_{\rm PTF}$ observations are shown, though we caution that iPTF 16abc may exhibit significant color evolution at this phase, in which case $g_{\rm PTF}$ would be a poor proxy for V. Each model light curve is translated to match the LCO observations ∼1.7 days after t_0 given the uncertain time of explosion. Translational offsets are listed in the bottom panel legend, which shows the models in order of decreasing ^{56}Ni from top to bottom, then left to right. The inset in the top panel shows the residuals relative to the W7 model.

is not observed. Thus, the subChDoubleDet model is incompatible with the observations. The sub-Chandrasekhar detonation (subChDet) provides a better match to the observations, though this model is not favored as a particularly realistic scenario (see above). Of the sub-Chandrasekhar models, the violent merger model (Merger) provides the best match to the observations, including the early rise and color evolution. In detail, however, this model does not match the early wiggles in the light curve, has consistently redder colors than iPTF 16abc, and requires $t_{\rm exp} \approx 2.3$ days prior to t_0. As such, we postulate that iPTF 16abc is not the result of a violent WD–WD merger.

For clarity, of the two pure deflagration models only N5def is shown; however, the evolution of N1600Cdef is very similar. While the pure deflagration models produce the bluest colors at early times, they are underluminous at times $> t_0 + 4$ days and already rapidly evolving toward the red at $\sim t_0 + 7$ (iPTF 16abc exhibits a nearly constant $(B-V)_0$ color for ∼19 days after t_0). Thus, we conclude that iPTF 16abc is not compatible with pure deflagrations.

Of the $M_{\rm Ch}$ models, the W7 model better matches the observations, as the N100 model features a faster rise and higher luminosity than what is observed. We explore delayed-detonation models in further detail below.

5.4. Interaction with Nearby, Unbound Material

To model SN 2011fe, Dessart et al. (2014) examined pulsational delayed-detonation (PDD) models as an explanation for some SNe Ia. Briefly, PDD models differ from "standard" delayed-detonation (DD) models in that the expansion of the WD during the initial deflagration phase leads to the release of unbound material. Following this pulsation, the bound material contracts, eventually triggering a subsequent detonation.[23] An important consequence of this progression for PDD models is that the unbound material expands and avoids burning, unlike DD models that typically leave no unburnt material. This results in significantly more carbon in the outer layers of the SN ejecta (Dessart et al. 2014).

Dessart et al. (2014) find that DD models are universally faint and red at early times, ∼24–48 hr after explosion, while the PDD models exhibit a faster rise and bluer colors. Briefly, this occurs in the PDD scenario because the collision with the unbound material surrounding the WD heats the outer layers of the SN ejecta. Importantly, the PDD models are nearly indistinguishable from DD models around peak and post-peak.

In Figure 10 we compare photometric observations of iPTF 16abc to the high-^{56}Ni yield DD and PDD models presented in Dessart et al. (2014).[24] DD and PDD models with $M_{\rm Ni}/M_\odot \lesssim 0.7$ and 0.5, respectively, fail to match the early luminosity and blue colors of iPTF 16abc. The PDD models provide a better match to the observations than the DD models. The PDD models evolve more rapidly toward blue colors and provide a better match to the g-band flux in the days after explosion. Furthermore, unlike the DD models, the PDD models exhibit strong C II lines that gradually disappear in the ∼1 week after explosion (Dessart et al. 2014). In detail, the early wiggles in the iPTF 16abc light curve are not matched by the PDD models, which exhibit more smooth variations. Furthermore, while the focus of this study is the early evolution of iPTF 16abc, the PDD models evolve more rapidly to the red post-peak than the observations. Nevertheless, the PDD models presented in Dessart et al. (2014) provide several attractive explanations for the unusual features in the early behavior of iPTF 16abc. Small adjustments to the PDD models (e.g., additional ^{56}Ni mixing, which Dessart et al. only explore for DD models) may better match iPTF 16abc.

5.5. Strong ^{56}Ni Mixing in the SN Ejecta

Having examined other possibilities, we now consider whether the early evolution of iPTF 16abc can be explained simply by invoking strong mixing in the SN ejecta. Strong mixing leads to a faster initial rise, as well as a more rapid evolution toward blue colors.

Figure 11 compares the models from Piro & Morozova (2016) to iPTF 16abc. The Piro & Morozova models employ a piston-driven explosion to explode a single WD progenitor model. As the piston explosion does not result in any nucleosynthesis, the distribution of ^{56}Ni in the ejecta must be prescribed by hand, which enables a study of the effects of mixing on the resulting SN emission. Each model employs a

[23] Dessart et al. (2014) note that the deflagration and detonation in their PDD models are artificially triggered.
[24] Available at https://www-n.oca.eu/supernova/snia/snia_ddc_pddel.html.

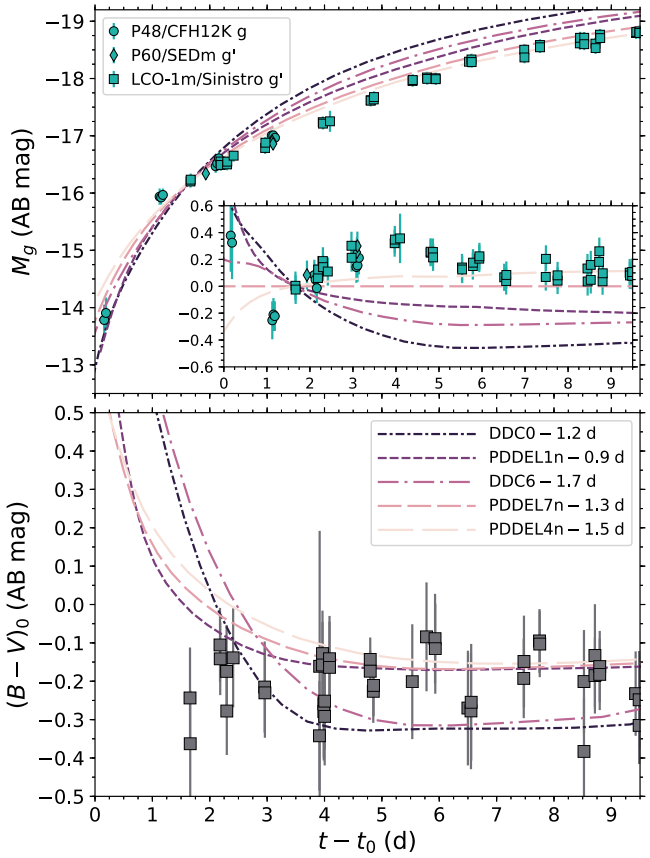

Figure 10. Same as Figure 9, but featuring the *g*-band light curve and the DD and PDD models from Dessart et al. (2014). The bottom panel legend lists the models in order of decreasing $M_{\rm Ni}$ from top to bottom. DD models (labeled as DDC to match the nomenclature of Dessart et al. 2014) are shown as dot-dashed lines, while PDD models (labeled as PDDEL) are shown as dashed lines. The inset in the top panel shows the residuals relative to the PDDEL7n model. The PDD models provide a better match to the observations.

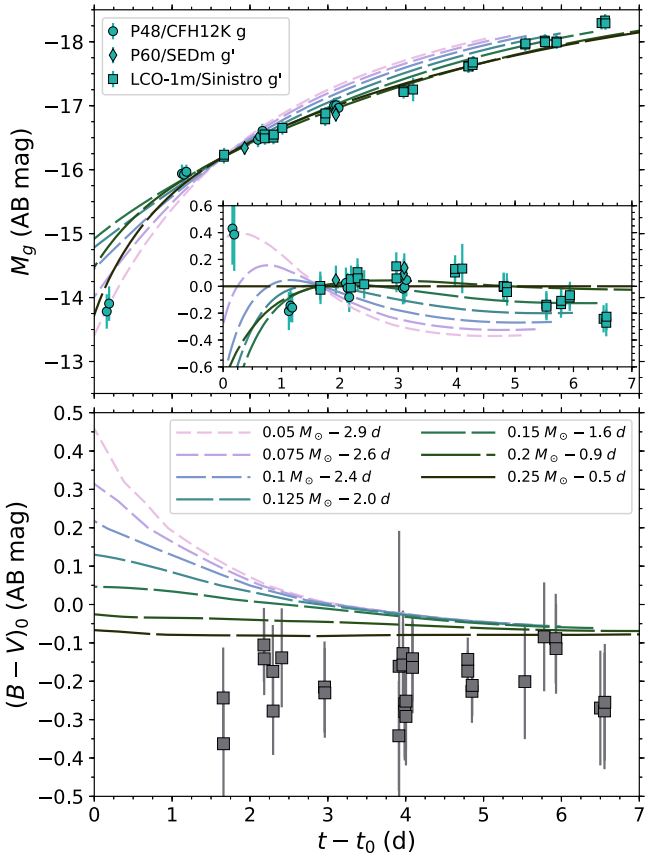

Figure 11. Same as Figure 9, but featuring the *g*-band light curve and models from Piro & Morozova (2016). The amount of ^{56}Ni mixing in the SN ejecta increases from the light, short-dashed lines to the dark, long-dashed lines. Unlike Figure 10, each model features the same $M_{\rm Ni}$, while the model names reflect the boxcar widths used to approximate the effects of mixing in the ejecta (see Piro & Morozova 2016). The top panel inset shows the residuals relative to the 0.25 $M_\odot$ model. The observations are best matched by the 0.25 $M_\odot$ model, i.e., the model with the most significant mixing.

fixed 0.5 $M_\odot$ of ^{56}Ni that has been distributed throughout the ejecta via boxcar averaging (see their Figure 1). The resulting light curves are synthesized using the SuperNova Explosion Code (SNEC; Morozova et al. 2015), as shown in Figure 11. Broadly speaking, the results can be summarized as follows: SNe with strong mixing exhibit a rapid rise and quickly develop blue colors, whereas models where the ^{56}Ni is confined to the innermost layers of the ejecta remain faint for days after explosion and feature a gradual color evolution from the red to the blue. The model with the strongest mixing (dark long-dashed line in Figure 11) best matches the observations of iPTF 16abc. This is the only model we have found that exhibits a flat $(B-V)_0$ color evolution in the days after explosion; however, in detail this model is too red relative to the observations of iPTF 16abc.

While the models from Piro & Morozova (2016) provide a good match to the optical photometric evolution of iPTF 16abc, they consistently overpredict the flux in the UV. They also overpredict the photospheric velocity of iPTF 16abc by ∼2–3000 km s^{-1}. Furthermore, the simple gray opacities in SNEC likely produce a faster rise and bluer colors than the more detailed treatments employed in Dessart et al. (2014) and Noebauer et al. (2017).

Both the PDD models and ejecta-mixing models show discrepancies with some early observations of iPTF 16abc. Nevertheless, we conclude that one, or both, of these scenarios, which feature qualitatively similar predictions, is the most likely explanation for iPTF 16abc. Indeed, it may be the case that the typical sequence of photometric and spectroscopic observations of young SNe Ia can never distinguish between these two possibilities (Noebauer et al. 2017).

6. The Emerging Sample of Young SNe Ia

The proliferation of high-cadence, time-domain surveys has led to several SNe Ia being discovered within ∼2 days of first light in roughly the past decade. Observations probing the early evolution of these SNe allow us to place unique constraints on their progenitor systems and the corresponding explosion physics. This has revealed diversity in the earliest epochs after explosion, and that commonly used SN Ia templates do not match observations at these phases (e.g., Foley et al. 2012).

In Section 4 we compared our early observations of iPTF 16abc to SN 2011fe, which has the most comprehensive observations of the young SN Ia sample. Given its normal spectroscopic and photometric evolution, SN 2011fe has been adopted as a standard for the early evolution of SNe Ia in many studies. While a detailed quantitative analysis is beyond the scope of this study, a qualitative examination of very young SNe Ia that otherwise exhibit normal spectra and evolution at

peak and post-peak[25] reveals considerable diversity. In other words, at early times SN 2011fe may not be the norm.

For SN 2011fe the initial rise is well described by a t^2 power law, the $(B-V)_0$ colors evolve from the red to the blue in the ~1 week after explosion, and the C II present in the initial spectra is weak (Nugent et al. 2011; Parrent et al. 2012; Zhang et al. 2016). In contrast, iPTF 16abc exhibits a near-linear rise in flux, the $(B-V)_0$ colors are blue and roughly constant, and the C II absorption is strong. Examining just these three qualitative features, SN 2009ig is well matched to SN 2011fe (Foley et al. 2012), while SN 2013dy (Zheng et al. 2013), SN 2017cbv (Hosseinzadeh et al. 2017), and iPTF 16abc all bear a striking resemblance. SN 2012cg, on the other hand, is intermediate to these two groups, with weak C II and a relatively shallow early rise, like SN 2011fe, but blue $(B-V)_0$ colors, like iPTF 16abc (Silverman et al. 2012; Marion et al. 2016). SN 2014J is intermediate in the other direction in that it exhibits a near-linear rise (Zheng et al. 2014; Goobar et al. 2015), but the color evolution is very similar to that of SN 2011fe (Amanullah et al. 2014).[26] That these early observations cannot be easily separated into two distinct groups suggests that it is unlikely that a single physical mechanism drives the diversity of SNe Ia at early times.

In the case of SN 2012cg and SN 2017cbv it has been argued that the early blue optical colors are indicative of interaction between the SN ejecta and a binary companion (Marion et al. 2016; Hosseinzadeh et al. 2017). SN 2017cbv is particularly remarkable in that the observations presented in Hosseinzadeh et al. (2017) show a clearly resolved bump in the U, B, and g' bands in the ~5 days after explosion. In Hosseinzadeh et al. it is found that the bump can be explained via the combination of ejecta–companion interaction and the normal evolution of an SN Ia. A challenge for this model, similar to iPTF 16abc (see Section 5.2), is that it significantly overpredicts the UV brightness of the SN compared to what is observed. Indeed, in the case of SN 2012cg, SN 2017cbv, and iPTF 16abc the UV–optical colors are significantly redder than those observed in iPTF 14atg. It is argued in Hosseinzadeh et al. (2017) that several model assumptions, including (i) ideal blackbody emission, (ii) a constant opacity, (iii) a simple power-law density profile for the ejecta, and (iv) spherical symmetry, may be incorrect, which could reconcile the discrepancy with the UV observations. Above, we argued for interaction with diffuse, unbound material and strong ^{56}Ni mixing as a possible explanation for iPTF 16abc, and indeed Hosseinzadeh et al. (2017) consider these possibilities for SN 2017cbv as well. Separately, several arguments against companion interaction for SN 2012cg are presented in Shappee et al. (2016b).

Ultimately, there are arguments in favor of and against each of the possibilities to model the early emission from SNe Ia. Moving forward, more detailed models and simulations are needed to properly explain the observed diversity. No matter the correct explanation for the early behavior of SN 2013dy, SN 2017cbv, and iPTF 16abc, the strong similarities between these events suggest that they may reflect a common physical origin.

[25] This definition excludes iPTF 14atg, which was shown to be subluminous with SN 2002es-like spectra (Cao et al. 2015).

[26] C II is not detected in the spectra of SN 2014J (Goobar et al. 2014; Zheng et al. 2014), though the earliest spectra of SN 2014J were obtained at a much later phase than the other SNe discussed here. Marion et al. (2015) find evidence for C I in the near-IR spectra of SN 2014J, but this detection cannot constrain the relative strength of C II and Si II shortly after explosion.

7. Conclusion

We have presented observations of the extraordinarily early discovery of the normal SN Ia iPTF 16abc. Our fast-response follow-up campaign allowed us to draw the following conclusions:

1. Extrapolation of the early light curve shows that the initial detection of iPTF 16abc occurred only $0.15\pm^{0.15}_{0.07}$ days after the time of first light, t_0.
2. We find no evidence for detectable signatures of SN shock cooling or the collision of the SN ejecta with a nondegenerate binary companion.
3. Assuming that $v_{\rm ph} \propto t^{-0.22}$, then $t_{\rm exp} \approx t_0$. A short dark phase, as this implies, is likely the result of either strong ^{56}Ni mixing or interaction of the SN ejecta with nearby, unbound material.
4. The strong and short-lived carbon features seen in the earliest spectra of iPTF 16abc can only be explained if there is incomplete burning. The pulsational delayed-detonation models presented in Dessart et al. (2014) produce C II absorption that is as strong as Si II at very early phases.
5. In contrast to SN 2011fe, $(B-V)_0$ is ~0.5 mag bluer for iPTF 16abc at $t \approx -16$ days. Furthermore, the $(B-V)_0$ colors of iPTF 16abc show no evolution over the first ~7 days of observations.
6. Finally, we show that the early light-curve evolution and colors of iPTF 16abc are best matched by the pulsational delayed-detonation models of Dessart et al. (2014) and the ejecta-mixing models of Piro & Morozova (2016).

Taken together, these observations suggest that the early emission from iPTF 16abc is due to the collision of the SN with nearby, unbound material and/or is significant mixing of ^{56}Ni in the SN ejecta. The PDD models from Dessart et al. (2014) are particularly attractive for explaining iPTF 16abc, because they produce strong C II absorption at early times. In the future, it would be useful to investigate more detailed PDD models that incorporate strong ^{56}Ni mixing to see whether they better replicate the observations of iPTF 16abc, as it is otherwise difficult to distinguish between these two scenarios.

Extremely early observations of young SNe provide a "smoking gun" to probe the mixing level in the ejecta, which, in turn, is a result of the explosion mechanism. Wide-field, high-cadence surveys, such as the Zwicky Transient Facility (Bellm 2016) and ATLAS (Tonry 2011, 2013), will discover a large number of very young SNe over the next few years, allowing us to extend our studies beyond single objects. While the sample of extremely young SNe Ia will grow by more than an order of magnitude, the detection of shock breakout cooling and ejecta–companion interaction will prove challenging. Given the diminutive size of WDs, the thermal emission following shock breakout can only be detected to ~10 Mpc on 1 m class telescopes. Furthermore, only ~10% of single-degenerate progenitors are expected to give rise to detectable emission following the collision of the SN ejecta with the binary companion (Kasen 2010). Despite these limitations, this study of iPTF 16abc shows that the early detection of SNe Ia may probe explosion physics by measuring the amount of mixing in the SN ejecta. Moving forward, a large sample of such objects will enable strict constraints on the proposed explosion mechanisms for SNe Ia.

Finally, we close by emphasizing the importance of fast-response photometric and spectroscopic follow-up campaigns. Without the early recognition of the youth of this SN and the associated follow-up, much of the analysis presented herein would not have been possible. The ability to trigger such observations is essential to improve our physical understanding of SNe Ia.

This study has benefited from the suggestions of an anonymous referee. We are deeply grateful to R. C. Thomas for indulging a slew of questions regarding C II in SNe. Similarly, it is our pleasure to buy a beer for R. Amanullah and U. Feindt for discussions regarding SALT2.

This paper utilizes the LCO infrastructure for rapid and regular monitoring of SNe, and we thank S. Valenti and I. Arcavi for their development efforts. Figure 3 would not have been possible without S. Blondin generously sharing the data from Blondin et al. (2012).

Much of the analysis presented herein would not have been possible without the help of several observers. We thank M. West for taking the first spectrum of iPTF 16abc as a ToO on the DCT. We also thank P. GuhaThakurta, E. C. Cunningham, K. A. Plant, H. Jang, and J. Torres for executing a Keck ToO as part of the UC/Caltech partnership, and also the Gemini service observers for executing our ToO observations. Additionally, J. Cohen, N. Suzuki, V. Ravi, R. Walters, A. Ho, H. Vedanthamand, K. De, and L. Yan helped obtain data for this paper.

A.A.M. is funded by the Large Synoptic Survey Telescope Corporation in support of the Data Science Fellowship Program. Y.C. acknowledges support from a postdoctoral fellowship at the eScience Institute, University of Washington.

D.A.H., C.M., and G.H. are supported by NSF-1313484.

The Intermediate Palomar Transient Factory project is a scientific collaboration among the California Institute of Technology, Los Alamos National Laboratory, the University of Wisconsin, Milwaukee, the Oskar Klein Center, the Weizmann Institute of Science, the TANGO Program of the University System of Taiwan, and the Kavli Institute for the Physics and Mathematics of the Universe. This work was supported by the GROWTH project funded by the National Science Foundation under grant no. 1545949. Part of this research was carried out at the Jet Propulsion Laboratory, California Institute of Technology, under a contract with NASA. This work makes use of observations from the LCO network. These results made use of the Discovery Channel Telescope at Lowell Observatory. Lowell is a private, nonprofit institution dedicated to astrophysical research and public appreciation of astronomy and operates the DCT in partnership with Boston University, the University of Maryland, the University of Toledo, Northern Arizona University, and Yale University. The upgrade of the DeVeny optical spectrograph has been funded by a generous grant from John and Ginger Giovale. Based on observations made with the Nordic Optical Telescope, operated by the Nordic Optical Telescope Scientific Association at the Observatorio del Roque de los Muchachos, La Palma, Spain, of the Instituto de Astrofísica de Canarias.

Facilities: DCT, Gemini:Gillett, Hale, Keck:I, Keck:II, LCOGT, PO:1.2m, PO:1.5m, NOT, VLT, *Swift*, OANSPM:HJT.

Software: `PTFIDE` (Masci et al. 2017), `FPipe`, `SALT2`, `SNID`, `lcogtsnpipe`, `UVOTSOURCE`.

Appendix
Photometric Light Curves

The full photometric light curves of iPTF 16abc are shown in Figure 12.

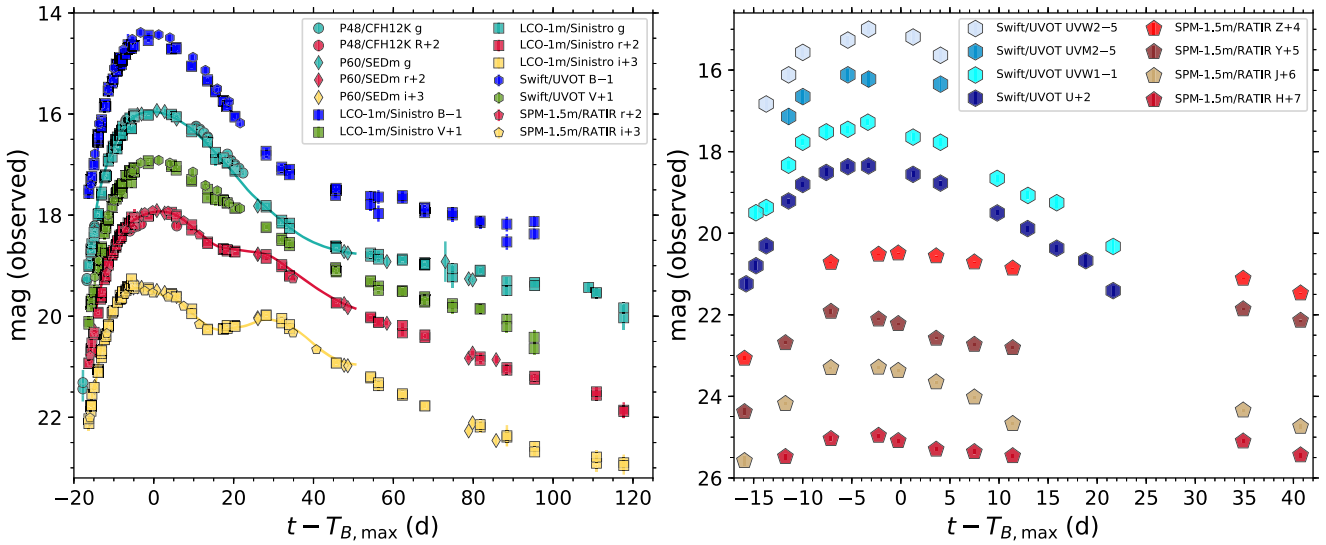

Figure 12. UV, optical, and near-IR light curves for iPTF 16abc. Left: *BVgri* light curves from the P48, P60, LCO-1 m, *Swift*, and SPM-1.5 m telescopes. The solid lines represent the best-fit model from SALT2 (see Section 3.3). Right: UV and near-IR light curves from the *Swift* and SPM-1.5 m telescopes, respectively. For both panels each light curve is represented with a different color, while the different symbols correspond to different instruments, as detailed in the legends. The legends also list offsets applied to each light curve. Photometry is shown in the AB mag system, with the exception of the *BV* bands, which are shown in the Vega system. These light curves have not been corrected for line-of-sight extinction.

ORCID iDs

A. A. Miller https://orcid.org/0000-0001-9515-478X
Y. Cao https://orcid.org/0000-0002-8036-8491
A. L. Piro https://orcid.org/0000-0001-6806-0673
N. Blagorodnova https://orcid.org/0000-0003-0901-1606
B. D. Bue https://orcid.org/0000-0002-7856-3570
S. B. Cenko https://orcid.org/0000-0003-1673-970X
R. Ferretti https://orcid.org/0000-0001-7814-5814
O. D. Fox https://orcid.org/0000-0003-2238-1572
C. Fremling https://orcid.org/0000-0002-4223-103X
D. A. Howell https://orcid.org/0000-0003-4253-656X
G. Hosseinzadeh https://orcid.org/0000-0002-0832-2974
M. M. Kasliwal https://orcid.org/0000-0002-5619-4938
R. R. Laher https://orcid.org/0000-0003-2451-5482
R. Lunnan https://orcid.org/0000-0001-9454-4639
F. J. Masci https://orcid.org/0000-0002-8532-9395
C. McCully https://orcid.org/0000-0001-5807-7893
P. E. Nugent https://orcid.org/0000-0002-3389-0586
J. Sollerman https://orcid.org/0000-0003-1546-6615
S. R. Kulkarni https://orcid.org/0000-0001-5390-8563

References

Adelman-McCarthy, J. K., Agüeros, M. A., Allam, S. S., et al. 2008, ApJS, 175, 297
Ahn, C. P., Alexandroff, R., Allende Prieto, C., et al. 2014, ApJS, 211, 17
Amanullah, R., Goobar, A., Johansson, J., et al. 2014, ApJL, 788, L21
Arnett, W. D. 1982, ApJ, 253, 785
Arnett, W. D., Branch, D., & Wheeler, J. C. 1985, Natur, 314, 337
Bellm, E. C. 2016, PASP, 128, 084501
Bertin, E., & Arnouts, S. 1996, A&AS, 117, 393
Betoule, M., Kessler, R., Guy, J., et al. 2014, A&A, 568, A22
Bianco, F. B., Howell, D. A., Sullivan, M., et al. 2011, ApJ, 741, 20
Bida, T. A., Dunham, E. W., Massey, P., & Roe, H. G. 2014, Proc. SPIE, 9147, 91472N
Blagorodnova, N., Neill, J. D., Walters, R., et al. 2017, arXiv:1710.02917
Blondin, S., Matheson, T., Kirshner, R. P., et al. 2012, AJ, 143, 126
Blondin, S., & Tonry, J. L. 2007, ApJ, 666, 1024
Bloom, J. S., Kasen, D., Shen, K. J., et al. 2012, ApJL, 744, L17
Branch, D., Chau Dang, L., & Baron, E. 2009, PASP, 121, 238
Branch, D., Dang, L. C., Hall, N., et al. 2006, PASP, 118, 560
Breeveld, A. A., Landsman, W., Holland, S. T., et al. 2011, in AIP Conf. Ser. 1358, ed. J. E. McEnery, J. L. Racusin, & N. Gehrels (Melville, NY: AIP), 373
Brown, P. J., Dawson, K. S., Harris, D. W., et al. 2012, ApJ, 749, 18
Butler, N., Klein, C., Fox, O., et al. 2012, Proc. SPIE, 8446, 844610
Cao, Y., Kulkarni, S. R., Howell, D. A., et al. 2015, Natur, 521, 328
Casali, M., Adamson, A., Alves de Oliveira, C., et al. 2007, A&A, 467, 777
Cenko, S. B., Cao, Y., Kasliwal, M., et al. 2016, ATel, 8909
Conley, A., Howell, D. A., Howes, A., et al. 2006, AJ, 132, 1707
Courtois, H. M., & Tully, R. B. 2015, MNRAS, 447, 1531
Dekker, H., D'Odorico, S., Kaufer, A., Delabre, B., & Kotzlowski, H. 2000, Proc. SPIE, 4008, 534
Dessart, L., Blondin, S., Hillier, D. J., & Khokhlov, A. 2014, MNRAS, 441, 532
Dhawan, S., Leibundgut, B., Spyromilio, J., & Blondin, S. 2016, A&A, 588, A84
Faber, S. M., Phillips, A. C., Kibrick, R. I., et al. 2003, Proc. SPIE, 4841, 1657
Ferretti, R., Amanullah, R., Goobar, A., et al. 2017, A&A, 606, A111
Fink, M., Kromer, M., Seitenzahl, I. R., et al. 2014, MNRAS, 438, 1762
Fitzpatrick, E. L. 1999, PASP, 111, 63
Foley, R. J., Challis, P. J., Filippenko, A. V., et al. 2012, ApJ, 744, 38
Fox, O. D., Kutyrev, A. S., Rapchun, D. A., et al. 2012, Proc. SPIE, 8453, 84531O
Fremling, C., Sollerman, J., Taddia, F., et al. 2016, A&A, 593, A68
Ganeshalingam, M., Li, W., & Filippenko, A. V. 2011, MNRAS, 416, 2607
Goobar, A., Johansson, J., Amanullah, R., et al. 2014, ApJL, 784, L12
Goobar, A., Kromer, M., Siverd, R., et al. 2015, ApJ, 799, 106
Guy, J., Astier, P., Baumont, S., et al. 2007, A&A, 466, 11
Hayden, B. T., Garnavich, P. M., Kasen, D., et al. 2010a, ApJ, 722, 1691
Hayden, B. T., Garnavich, P. M., Kessler, R., et al. 2010b, ApJ, 712, 350
Hodgkin, S. T., Irwin, M. J., Hewett, P. C., & Warren, S. J. 2009, MNRAS, 394, 675
Hook, I. M., Jørgensen, I., Allington-Smith, J. R., et al. 2004, PASP, 116, 425
Hosseinzadeh, G., Sand, D. J., Valenti, S., et al. 2017, ApJL, 845, L11
Im, M., Choi, C., Yoon, S.-C., et al. 2015, ApJS, 221, 22
Kasen, D. 2010, ApJ, 708, 1025
Kromer, M., Fremling, C., Pakmor, R., et al. 2016, MNRAS, 459, 4428
Law, N. M., Kulkarni, S. R., Dekany, R. G., et al. 2009, PASP, 121, 1395
Levanon, N., Soker, N., & García-Berro, E. 2015, MNRAS, 447, 2803
Littlejohns, O. M., Butler, N. R., Cucchiara, A., et al. 2014, AJ, 148, 2
Maoz, D., Mannucci, F., & Nelemans, G. 2014, ARA&A, 52, 107
Marion, G. H., Brown, P. J., Vinkó, J., et al. 2016, ApJ, 820, 92
Marion, G. H., Sand, D. J., Hsiao, E. Y., et al. 2015, ApJ, 798, 39
Masci, F. J., Laher, R. R., Rebbapragada, U. D., et al. 2017, PASP, 129, 014002
Miller, A. A., Laher, R., Masci, F., et al. 2016, ATel, 8907
Morozova, V., Piro, A. L., Renzo, M., et al. 2015, ApJ, 814, 63
Mould, J. R., Huchra, J. P., Freedman, W. L., et al. 2000, ApJ, 529, 786
Noebauer, U. M., Kromer, M., Taubenberger, S., et al. 2017, MNRAS, 472, 2787
Nomoto, K., Thielemann, F.-K., & Yokoi, K. 1984, ApJ, 286, 644
Nugent, P. E., Sullivan, M., Cenko, S. B., et al. 2011, Natur, 480, 344
Ofek, E. O., Laher, R., Surace, J., et al. 2012, PASP, 124, 854
Oke, J. B., Cohen, J. G., Carr, M., et al. 1995, PASP, 107, 375
Olling, R. P., Mushotzky, R., Shaya, E. J., et al. 2015, Natur, 521, 332
Parrent, J. T., Howell, D. A., Friesen, B., et al. 2012, ApJL, 752, L26
Parrent, J. T., Thomas, R. C., Fesen, R. A., et al. 2011, ApJ, 732, 30
Phillips, M. M. 1993, ApJL, 413, L105
Phillips, M. M., Simon, J. D., Morrell, N., et al. 2013, ApJ, 779, 38
Piro, A. L., Chang, P., & Weinberg, N. N. 2010, ApJ, 708, 598
Piro, A. L., & Morozova, V. S. 2016, ApJ, 826, 96
Piro, A. L., & Nakar, E. 2014, ApJ, 784, 85
Poznanski, D., Prochaska, J. X., & Bloom, J. S. 2012, MNRAS, 426, 1465
Rabinak, I., & Waxman, E. 2011, ApJ, 728, 63
Rahmer, G., Smith, R., Velur, V., et al. 2008, Proc. SPIE, 7014, 70144Y
Schlafly, E. F., & Finkbeiner, D. P. 2011, ApJ, 737, 103
Seitenzahl, I. R., Ciaraldi-Schoolmann, F., Röpke, F. K., et al. 2013, MNRAS, 429, 1156
Shappee, B. J., Piro, A. L., Holoien, T. W.-S., et al. 2016a, ApJ, 826, 144
Shappee, B. J., Piro, A. L., Stanek, K. Z., et al. 2016b, arXiv:1610.07601
Silverman, J. M., & Filippenko, A. V. 2012, MNRAS, 425, 1917
Silverman, J. M., Ganeshalingam, M., Cenko, S. B., et al. 2012, ApJL, 756, L7
Skrutskie, M. F., Cutri, R. M., Stiening, R., et al. 2006, AJ, 131, 1163
Stritzinger, M., Leibundgut, B., Walch, S., & Contardo, G. 2006, A&A, 450, 241
Theureau, G., Hanski, M. O., Coudreau, N., Hallet, N., & Martin, J.-M. 2007, A&A, 465, 71
Thomas, R. C., Aldering, G., Antilogus, P., et al. 2007, ApJL, 654, L53
Thomas, R. C., Aldering, G., Antilogus, P., et al. 2011, ApJ, 743, 27
Tonry, J. L. 2011, PASP, 123, 58
Tonry, J. L. 2013, RSPTA, 371, 20120269
Valenti, S., Howell, D. A., Stritzinger, M. D., et al. 2016, MNRAS, 459, 3939
Vernet, J., Dekker, H., D'Odorico, S., et al. 2011, A&A, 536, A105
Watson, A. M., Richer, M. G., Bloom, J. S., et al. 2012, Proc. SPIE, 8444, 84445L
Whelan, J., & Iben, I., Jr. 1973, ApJ, 186, 1007
Zacharias, N., Finch, C. T., Girard, T. M., et al. 2013, AJ, 145, 44
Zhang, K., Wang, X., Zhang, J., et al. 2016, ApJ, 820, 67
Zheng, W., Shivvers, I., Filippenko, A. V., et al. 2014, ApJL, 783, L24
Zheng, W., Silverman, J. M., Filippenko, A. V., et al. 2013, ApJL, 778 L15